

## Conference Paper

# Turbulence Quantification in Supercritical Nitrogen Injection: An Analysis of Turbulence Models

Leandro Magalhães, Francisco Carvalho, André Silva, and Jorge Barata

Universidade da Beira Interior

## Abstract

In Liquid Rocket Engines, higher combustion efficiencies come at the cost of the propellants exceeding their critical point conditions and entering the supercritical domain. The term fluid is used because, under these conditions, there is no longer a clear distinction between a liquid and a gas phase. The non-conventional behavior of thermophysical properties makes the modeling of supercritical fluid flows a most challenging task. In the present work, a RANS computational method following an incompressible but variable density approach is devised on which the performance of several turbulence models is compared in conjunction with a high accuracy multi-parameter equation of state. Also, a suitable methodology to describe transport properties accounting for dense fluid corrections is applied. The results are validated against experimental data, becoming clear that there is no trend between turbulence model complexity and the quality of the produced results. For several instances, one- and two- equation turbulence models produce similar and better results than those of Large Eddy Simulation (LES). Finally, considerations about the applicability of the tested turbulence models in supercritical simulations are given based on the results and the structural nature of each model.

**Keywords:** Supercritical fluids, RANS turbulence modeling, Liquid rocket engines

Corresponding Author:  
Leandro Magalhães  
leandro.magalhaes@ubi.pt

Received: 26 November 2019  
Accepted: 13 May 2020  
Published: 2 June 2020

Publishing services provided by  
Knowledge E

© Leandro Magalhães et al. This article is distributed under the terms of the [Creative Commons Attribution License](#), which permits unrestricted use and redistribution provided that the original author and source are credited.

Selection and Peer-review under the responsibility of the ICEUBI2019 Conference Committee.

## 1. Introduction

Supercritical fluids exist on Earth as a byproduct of naturally occurring phenomena, i.e., crystal formation in aqueous solutions at supercritical conditions. The dynamics of these fluids is still a topic of study, and its implications are not fully understood. Despite that, the RS-25, the Vulcain, and the Vinci engines are a few examples of Liquid Rocket Engines (LRE's) where conditions in the combustion chamber exceed those of the critical point [1].

With increasing development costs for the future and improved rocket engines, there is a need to eliminate the trail-and-errors phase of the development. With enormous demands and competitions for cheaper and safer launchers access to space, the design

## OPEN ACCESS

of advanced reusable launching vehicles (RLV) is required to have a higher payload-to-cost ratio, while maintaining reliability.

In the combustion chamber of the RS-25 engine, for example, the operating pressure of 20.6 MPa exceeds the critical pressure of oxygen (4.96 MPa) and, as the cryogenic oxygen injection temperature increases, passing the critical point, it becomes a supercritical fluid. As the temperature increases even further, the liquid-like supercritical oxidizer crosses the pseudo-boiling line and transitions to a gas-like fluid. Here, the isothermal vaporization phenomenon typical of subcritical fluids is replaced by a continuous non-equilibrium process where the change in enthalpy has both a structural and thermal component. Density experiences a sharp drop over a minimal temperature interval, and the specific heat reaches a maximum that tends to infinity as the pseudo-boiling line gets closer to the critical point [2]. The two parameters  $\frac{\partial \rho}{\partial T}$  and  $c_{pmax}$  can therefore be used to identify pseudo-boiling temperatures for different pressure values as shown in Figure 1. For nitrogen, it is visible that as the pressure approximates the critical value of 3.39 MPa, the peak in specific heat becomes more noticeable along with the slope of  $\frac{\partial \rho}{\partial T}$ .

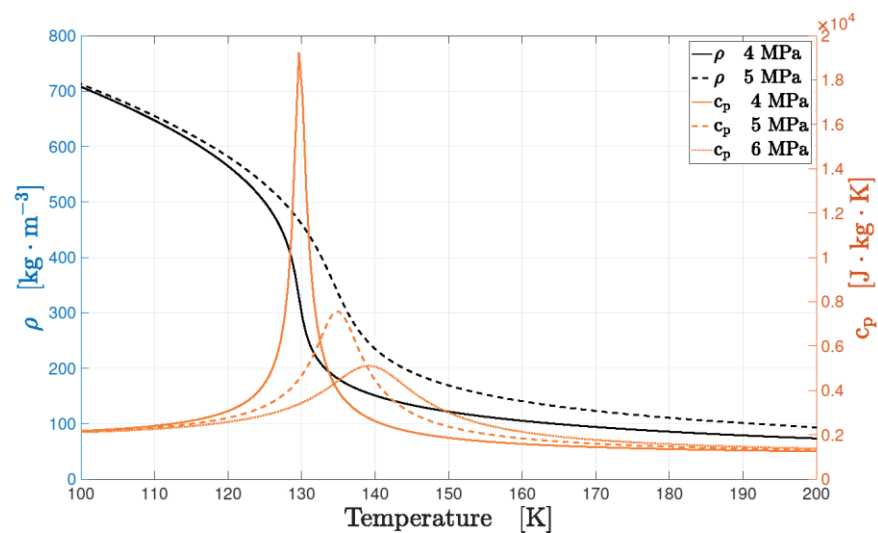


Figure 1: Density and isobaric specific heat values for nitrogen [3].

In this regime, the ideal gas Equation of State (EoS) must be replaced by more accurate formulations. While multi-parameter EoS have high accuracy, they fall behind in terms of computational efficiency. To overcome this obstacle, in the present work, density values are loaded from a preexisting real gas library [4], based on a reference equation of state for nitrogen [5] allowing for an increased accuracy at a reduced computational cost, since look-up tables are generated prior to the computations, effectively removing the need for thermophysical properties to be calculated in each iteration. The non-linearity

of transport variables must also be accurately defined, and the equations proposed by [6] are used.

Concerning the turbulence model employed to evaluate turbulent stresses present in the conservation equations for momentum and energy, a considerable amount of care must be employed. Turbulence is regarded as the last unsolved problem of classical physics. The presence of advective terms in the governing equations leads to their admittance of a chaotic solution after a critical Reynolds number. Modeling is then performed resorting to techniques such as RANS - Reynolds Averaged Navier Stokes (where FANS - Favre Averaged Navier Stokes is also included), LES - Large Eddy Simulation or DNS - Direct Numerical Simulation. However, when discussing supercritical fluid flows, the fact that no turbulence models developed explicitly for flows at these conditions exist, is an added factor of uncertainty.

The DNS technique, albeit potentially the most accurate it is also the most expensive. As such, the level of accuracy desired for a given application may render it the least efficient method. Nevertheless, it has been used by [7] at a reduced Reynolds number, while, on the other hand, [8] employed a RANS based averaging procedure. LES appears to be the most used technique, [9-16]. Nevertheless, it has failed to systematically outperform RANS-based solvers.

Our objective is to evaluate several turbulence models in a RANS based numerical solver to access the necessary complexity of the said model in providing accurate results of the centerline density distribution for a nitrogen mixing layer. With an appropriate thermodynamic model, the applicability of several turbulence models to supercritical flows is studied along with its cost/accuracy ratio. The same issue was dealt with by [17], not by changing the turbulence model, but by reassessing the concept of a variable turbulent Prandtl number, applied to the standard K- $\epsilon$  turbulence model.

The test conditions (cases 3 and 4) from [18] listed in Table 1 are used as the base on which the mathematical and numerical framework is built upon. Table 1 details injection and chamber conditions, namely pressure ( $p_\infty$ ), temperature ( $T_\infty$ ) and specific mass ( $\rho_\infty$ ), as well as injection velocity ( $u_0$ ), temperature ( $T_0$ ) and specific mass ( $\rho_0$ ).

TABLE 1: Test conditions [18].

Case	$p_\infty$ [MPa]	$u_0$ [m/s]	$T_0$ [K]	$T_\infty$ [K]	$\rho_0$ [kg/m <sup>3</sup> ]	$\rho_\infty$ [kg/m <sup>3</sup> ]
3	3.97	4.9	126.9	297	457.82	45.24
4	3.98	5.4	137	297	164.37	45.36

The next few sections describe the physical and numerical models employed. The governing equations are initially introduced, followed by a summary of the turbulence

models to be tested. The models used to approximate the values of transport properties are then introduced, after which the numerical methods implemented to translate the mathematical model to a discrete domain with the least possible amount of numerical error are described.

## 2. Governing Equations

The Favre averaged conservation equations for mass, momentum, and energy constitute the backbone of the model employed and are reproduced here in equations (1) to (3), respectively. Lastly, a steady-state is considered in this variable density but incompressible approach.

$$\frac{\partial}{\partial x_i}(\bar{\rho}\tilde{u}_i) = 0 \quad (1)$$

$$\frac{\partial}{\partial x_j}(\bar{\rho}\tilde{u}_i\tilde{u}_j) = -\frac{\partial\bar{p}}{\partial x_i} + \frac{\partial}{\partial x_j}(\bar{t}_{ij} + \tau_{ij}) = \bar{\rho}f_i \quad (2)$$

$$\frac{\partial}{\partial x_j}(\bar{\rho}\tilde{u}_j\tilde{H}) = \frac{\partial}{\partial x_j} \left[ \left( \frac{\mu}{Pr} + \frac{\mu_t}{Pr_t} \right) \frac{\partial\tilde{h}}{\partial x_j} + \tilde{u}_i(\bar{t}_{ij} + \tau_{ij}) \right] \quad (3)$$

## 3. Turbulence models

Starting from the Boussinesq approach (the relationship between Reynolds' stresses and the average rate of strain is similar to the Newtonian relationship between viscous stresses and the rate of strain), modeling of the Reynolds stress tensor ( $\tau_{ij}$ ) originated from the averaging process must be approximated. Of the six turbulence models tested, five of them are based on this eddy viscosity concept.

The Spalart-Allmaras model [19] is a one-equation model in which a direct derivation of an equation for the transport of the modified eddy viscosity is performed. This does not happen on the  $K-\epsilon$  based models [20], [21] and [22] where transport equations for both the turbulent kinetic energy ( $K$ ) and its dissipation rate ( $\epsilon$ ) are introduced. In the  $K-\omega$  based models, the dissipation of turbulent kinetic energy is replaced by the specific dissipation rate, and as such, a variation of the model of [23] is considered. All the models reasoned insofar are based on Boussinesq's eddy viscosity concept. However, another one is considered, which does not have this concept as its underlying relationship. The Stress Baseline (BSL) model [24] closes the system of governing equations with transport equations for  $\omega$  and  $\tau_{ij}$ .

## 4. Equation of State and Transport Properties

The REFPROPv9.1 [4] database is used to achieve a high level of accuracy at a reduced computational cost. In this way, a multi-parameter equation of state [5], based on the Helmholtz free energy, for nitrogen is used to generate the look-up table.

The methodology proposed by [6] is used for the calculation of transport properties – equations (4) and (5) for viscosity and thermal conductivity, respectively. The components  $\mu^0(T)$  and  $\lambda^0(T)$  define the dilute gas contributions, while the components  $\mu^r(\tau, \delta)$  and  $\lambda^r(\tau, \delta)$  represent departure functions accounting for dense fluid behavior as a function of both reduced temperature and density –  $\tau$  and  $\delta$ , respectively. The thermal conductivity has an additional term to account for the singular behavior in the critical point, that is, its evolution to infinity, labeled critical enhancement  $\lambda^c(\tau, \delta)$ .

$$\mu = \mu^0(T) + \mu^r(\tau, \delta) \quad (4)$$

$$\lambda = \lambda^0(T) + \lambda^r(\tau, \delta) + \lambda^c(\tau, \delta) \quad (5)$$

## 5. Boundary Conditions

The geometry corresponding to the experimental setup of [18] is represented in Figure 2. The diameter of the chamber and the injector are of 122 mm and 2.2 mm, respectively, while measuring, in length, 250 mm and 90 mm. Liquid nitrogen is injected into a chamber filled with gaseous nitrogen according to the conditions indicated in Table 1.

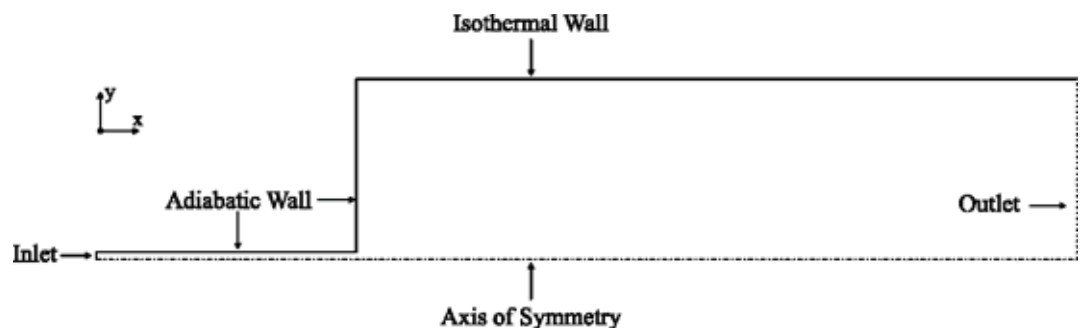


Figure 2: Boundary conditions for the physical model.

The domain contains five different boundary conditions, also defined in Figure 2. A constant axial velocity profile is set at the inlet and the radial velocity is set to zero. At the walls, a no-slip condition is applied where both the normal and tangential velocity are set to zero. In the adiabatic walls, the heat flux is set to zero, but for the isothermal wall, constant temperature of 297 K is imposed.

## 6. Numerics

A pressure-based algorithm is implemented where conservation of mass is implicitly achieved through a pressure-based continuity equation, obtained by taking the divergent of the momentum equations (2) and introducing the condition  $\frac{\partial}{\partial x_i}(\bar{\rho}\tilde{u}_i) = 0$ . A system of equations comprising this and the momentum equations is solved to obtain the velocity and pressure fields simultaneously. Energy and transport equations for turbulent variables are solved until convergence is reached.

A Finite Volume Method (FVM) is employed, and the values of the arbitrary scalar  $\varphi$  are stored at cell-centers. For the current test conditions, [8] suggests at least a second-order upwind (SOU) scheme to interpolate the face values of the control volumes for the advective terms. However, the QUICK scheme [25] is used instead to guarantee a more stable behavior and a third-order accuracy. The diffusive terms are discretized using a second-order central differencing scheme. Finally, the pressure values in equation [2] are obtained directly from the mesh faces by implementing a staggered grid method through the PPressure STaggering Option (PRESTO!) [26] thus mitigating the occurrence of oscillations in the pressure field. Implicit relaxation is applied to the governing equations through a pseudo-time-step method [26] to improve stability.

A hybrid initialization method [26] is employed where the inlet velocity is set to  $u_0$  from Table 1 and the absolute pressure at the outlet is set to  $p_\infty$ . The velocity and pressure fields calculated with this method are then introduced in the first cycle of the pressure-based algorithm. Grid independence is achieved at 18000 points, using a rectangular mesh.

## 7. Results and Discussion

Figure 3 depicts a comparison of the results obtained for the centerline density decay when using the turbulence models described for case 3. It is visible that almost all models predict a potential core with values ranging between  $x/d = 6.4$  and  $x/d = 7.6$ . The only exception is the standard  $K-\omega$  model that largely overestimates the length of the potential core to  $x/d = 12.5$ , which can be attributed to the poor performance of this model in free-stream conditions. Even if the version here tested is an improvement over the 1998 Wilcox  $K-\omega$  model, with an added cross-diffusion term introduced specifically to deal with the free-stream sensitivity, it does not provide acceptable results throughout the whole of the domain.

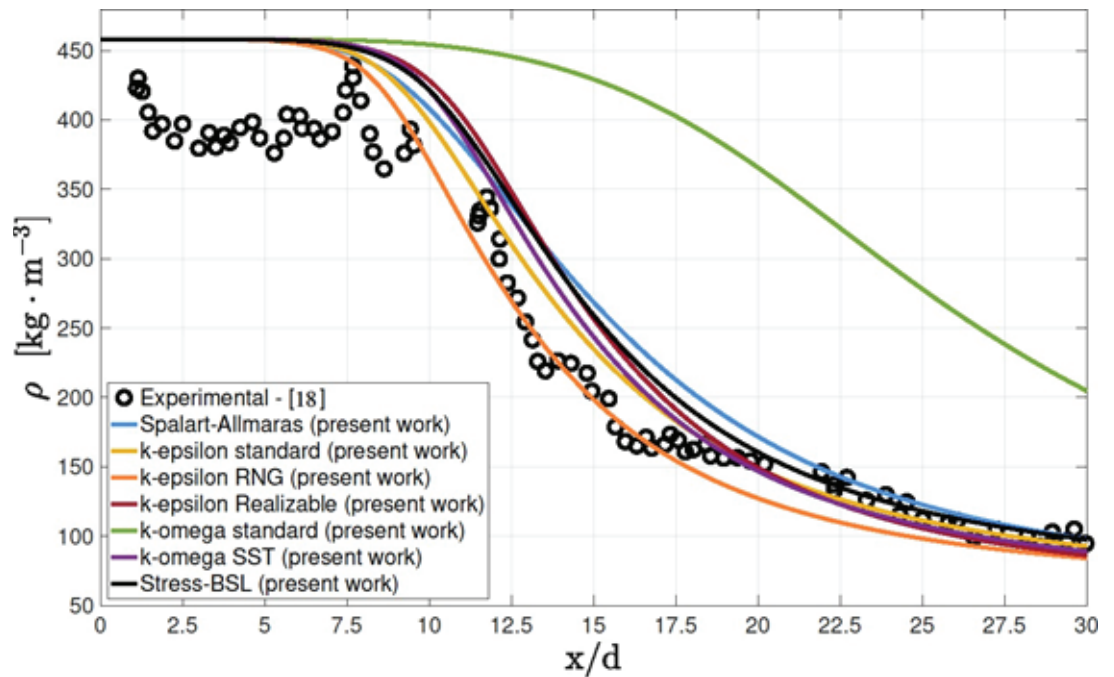


**Figure 3:** Centerline density decay in case 3 with different turbulence models and REFPROPv9.1.

The density values predicted in this region are higher than those of the experimental data, but this can be a result of the measuring procedure used by [18]. Raman spectroscopy works by directing a monochromatic laser at the test substance and measuring the scattered radiation using a sensor. However, for higher densities, the jet tends to deflect the radiation along the axial direction, thus decreasing signal intensity at the sensor. As density reduces, this phenomenon is no longer predominant.

Turbulence seems not to influence the potential core. However, when entering the transition region, instabilities start to appear, and turbulent dissipation begins to increase. [27] reports a maximum of density fluctuations in this region as pockets of dense fluid start to smear the potential core. When this happens, the fluid crosses the pseudo-boiling line leading to thermal expansion and reduced shearing, resulting in turbulence dissipation, as depicted in Figure 4, starting to decrease around  $x/d=15$ . This thermal expansion also appears to spawn sharp velocity fluctuations visible in the increase of turbulent kinetic energy, indicative of a robust turbulent mixing mechanism.

In this region, the more elaborate structure of the SST  $k-\omega$  does not provide outstanding results despite being based on the more recent Wilcox 2006 model [28] and having a shear-stress based formulation for eddy viscosity. When moving away from the wall,  $\mu_t$  returns to  $\bar{\rho}k/\omega$ , and the model only uses the  $K-\epsilon$  based coefficients. Consequently, we can see that its results more closely match those of the  $K-\epsilon$  variants than those of the standard  $K-\omega$ .

The five equation Stress-BSL model also overestimates the density values between  $7.5 < x/d < 20$ , which could be related, in part, to the dependency of this model on  $\omega$  and the inherent deficiencies of its transport equation. The one equation Spalart-Allmaras leads to a similar overestimation of density values between  $7.5 < x/d < 22.5$ , but it is striking to see how well this simple formulation stacks against a five-equation model.

In the three  $\epsilon$  based models, the realizable variant provides the worst results since the beginning of the transition zone up to  $x/d = 20$ . It seems that the realisability constraint and the alternative  $\epsilon$  transport equation do not give any visible contributions. Between the standard and the RNG  $K-\epsilon$ , there are two main differences: the formulation for the destruction of the turbulent dissipation rate and the definition for the turbulent Prandtl number inserted into the energy equation and in the turbulent variables transport equations. Especially when considering the work from [17], we are led to believe that the variable turbulent Prandtl number is the leading cause for an improved behavior of the RNG  $K-\epsilon$  model over the standard version. The model accurately predicts the density values across the domain.

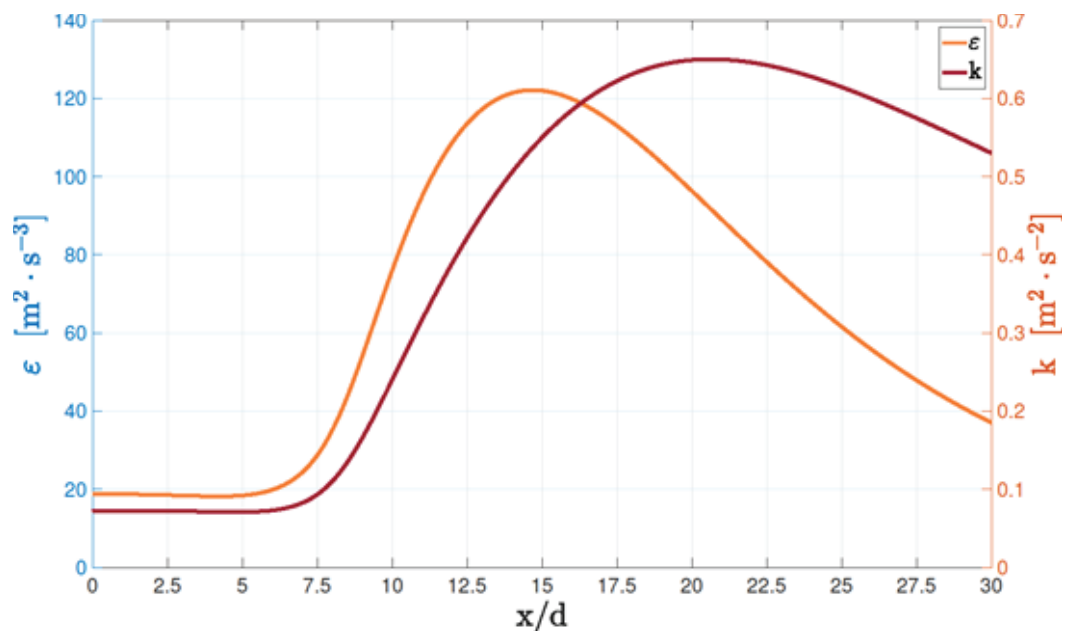


**Figure 4:** Centerline distribution of the turbulent dissipation rate and kinetic energy in case 3 with the RNG  $K-\epsilon$  model.

In case 4, the differences in potential core length, depicted in Figure 5, are similar to those of case 3, ranging from  $x/d=6.6$  to  $x/d=7.7$  with the standard  $K-\omega$  being once again the exception. Injection density is considerably reduced in this case when compared to that of case 3, and, therefore, there is no longer an apparent density overestimation in the potential core. However, an unrealistic potential core is still predicted independently of the turbulence model. In this case, the Stress-BSL model is the only one to correctly

predict density values between  $17.5 < x/d < 30$  while the remaining ones provide a slight under prediction. Nevertheless, its behavior outside this region is not exceptional, and the overall results do not justify the additional computational cost. Results from the RNG K- $\epsilon$  continue to be acceptable, but there is also an improvement from the standard K- $\epsilon$  and the Spalart-Allmaras models for which the outcome is nearly identical.

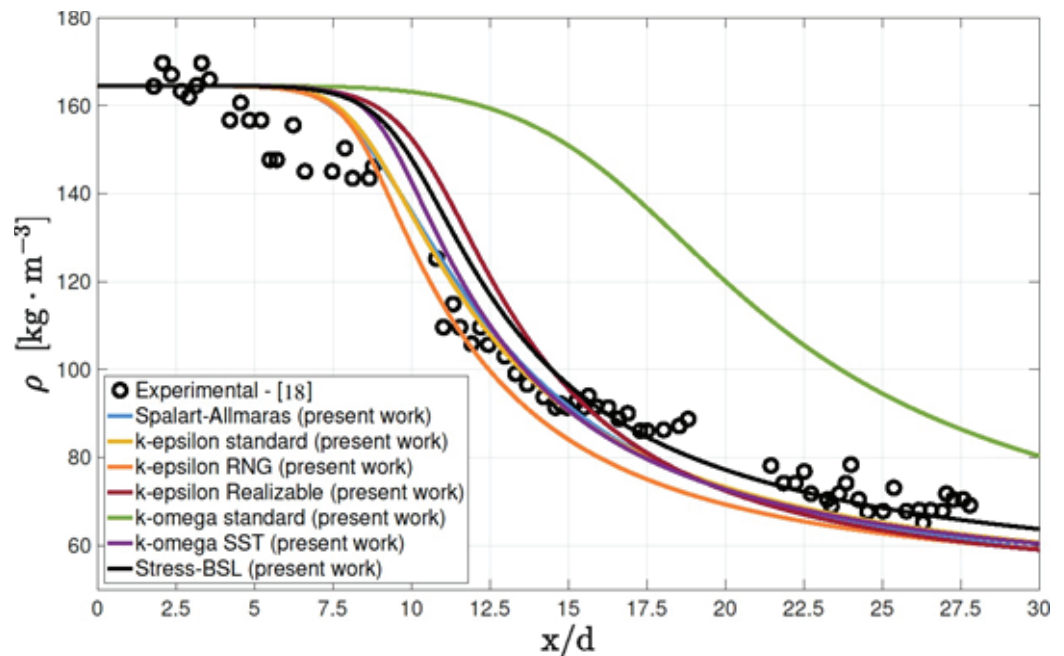


Figure 5: Centerline density decay in case 4 with different turbulence models and REFPROPv9.1

## 8. Conclusions

In the present study, the injection of liquid-like supercritical nitrogen into a gaseous nitrogen- filled chamber is simulated for two different test conditions. The system of governing equations is closed by six different models that are either based on the concept of eddy viscosity or the transport of the Reynolds stresses.

The results obtained with a second-order turbulence model show that there is no clear advantage in calculating higher-order turbulent correlation terms, indicating that their relevance under these conditions is minimal. Also, the blending functions and shear stress transport formulation for  $\mu_t$  of the SST K- $\omega$  model do not contribute to improving predictions since the flow is mainly in a free-stream region. The RNG K- $\epsilon$  model offers the best results for case 3, possibly due to the variable turbulent Prandtl number but the similarly good results obtained for case 4 with the Spalart-Allmaras and the Standard K- $\epsilon$  models indicate that there may be other relevant factors.

Therefore, the results here obtained are indicative that there is no direct correlation between the turbulence model complexity and quality of the results, in what supercritical fluid flows are concerned.

Having determined how the velocity field affects the flow structure, one of the next steps is, therefore, to determine the impact of a heating mechanism inside the injector and the correct boundary conditions to be used.

## Aknowledgements

The present work was performed under the scope of the Aeronautics and Astronautics Research Center (AEROG) of the Laboratório Associado em Energia, Transportes e Aeronáutica (LAETA) activities and it was supported by Fundação para a Ciência e Tecnologia (FCT) through grant number SFRH/BD/136381/2018 and project number UID/EMS/50022/2019.

## References

- [1] D. Haeseler, F. Haidinger, L. Brummer, J. Haberle and P. Luger, "Development and Testing Status of the Vinci Thrust Chamber," in *48th AIAA/ASME/SAE/ASEE Joint Propulsion Conference & Exhibit*, 2012.
- [2] D. Banuti, M. Raju, P. C. Ma, M. Ihme and J. Hickey, "Seven questions about supercritical fluids - towards a new fluid state diagram," in *55th AIAA Aerospace Sciences Meeting*, 2017.
- [3] M. O. McLinden, E. W. Lemmon and M. L. Huber, "NIST Thermodynamic and Transport Properties REFPROP, Version 7.0," *NIST Standard Reference Database 23*, 2002.
- [4] E. W. Lemmon, I. H. Bell, M. L. Huber and M. O. McLinden, *NIST Standard Reference Database 23: Reference Fluid Thermodynamic and Transport Properties-REFPROP, Version 10.0*, National Institute of Standards and Technology, 2018.
- [5] R. Span, E. W. Lemmon, R. T. Jacobsen, W. Wagner and A. Yokozeki, "A Reference Equation of State for the Thermodynamic Properties of Nitrogen for Temperatures from 63.151 to 1000 K and Pressures to 2200 MPa," *Journal of Physical and Chemical Reference Data*, vol. 29, pp. 1361-1433, 11 2000.
- [6] E. W. Lemmon and R. T. Jacobsen, "Viscosity and Thermal Conductivity Equations for Nitrogen, Oxygen, Argon, and Air," *International Journal of Thermophysics*, vol. 25, pp. 21-69, 1 2004.

- [7] F. Ries, P. Obando, I. Shevchuck, J. Janicka and A. Sadiki, "Numerical analysis of turbulent flow dynamics and heat transport in a round jet at supercritical conditions," *International Journal of Heat and Fluid Flow*, vol. 66, pp. 172-184, 8 2017.
- [8] T. S. Park, "LES and RANS simulations of cryogenic liquid nitrogen jets," *The Journal of Supercritical Fluids*, vol. 72, pp. 232-247, 12 2012.
- [9] T. Schmitt, L. Selle, B. Cuenot and T. Poinso, "Large-Eddy Simulation of transcritical flows," *Comptes Rendus Mécanique*, vol. 337, pp. 528-538, 6 2009.
- [10] T. Schmitt, L. Selle, A. Ruiz and B. Cuenot, "Large-Eddy Simulation of Supercritical-Pressure Round Jets," *AIAA Journal*, vol. 48, pp. 2133-2144, 9 2010.
- [11] M. Jarczyk and M. Pfitzner, "Large Eddy Simulation of Supercritical Nitrogen Jets," in *50th AIAA Aerospace Sciences Meeting including the New Horizons Forum and Aerospace Exposition*, 2012.
- [12] C. A. Niedermeier, M. Jarczyk, S. Hickel, N. Adams and M. Pfitzner, "Large-Eddy Simulation of Turbulent Trans- and Supercritical Mixing," in *21st AIAA Computational Fluid Dynamics Conference*, 2013.
- [13] J. Hickey, P. C. Ma, M. Ihme and S. S. Thakur, "Large Eddy Simulation of Shear Coaxial Rocket Injector: Real Fluid Effects," in *49th AIAA/ASME/SAE/ASEE Joint Propulsion Conference*, 2013.
- [14] X. Petit, G. Ribert, G. Lartigue and P. Domingo, "Large-eddy simulation of supercritical fluid injection," *The Journal of Supercritical Fluids*, vol. 84, pp. 61- 73, 12 2013.
- [15] H. Mueller, C. A. Niedermeier, M. Jarczyk, M. Pfitzner, S. Hickel and N. A. Adams, "Large-eddy simulation of trans- and supercritical injection," in *Progress in Propulsion Physics*, 2016.
- [16] S. Taghizadeh and D. Jarrahbashi, "Proper Orthogonal Decomposition Analysis of Turbulent Cryogenic Liquid Jet Injection Under Transcritical and Supercritical Conditions," *Atomization and Sprays*, vol. 28, pp. 875-900, 2018.
- [17] L. Magalhães, A. Silva and J. Barata, "Locally variable turbulent Prandtl number considerations on the modeling of Liquid Rocket Engines operating above the critical point," *ILASS–Europe 2019, 29th Conference on Liquid Atomization and Spray Systems, 2-4 September 2019, Paris, France*, 2019.
- [18] W. Mayer, J. Telaar, R. Branam, G. Schneider and J. Hussong, "Raman Measurements of Cryogenic Injection at Supercritical Pressure," *Heat and Mass Transfer*, vol. 39, pp. 709-719, 7 2003.
- [19] P. Spalart and S. Allmaras, "A one-equation turbulence model for aerodynamic flows," in *30th Aerospace Sciences Meeting and Exhibit*, 1992.

- [20] B. E. Launder and D. B. Spalding, Lectures in mathematical models of turbulence, London, England: Academic Press, 1972.
- [21] V. Yakhot, S. A. Orszag, S. Thangam, T. B. Gatski and C. G. Speziale, "Development of turbulence models for shear flows by a double expansion technique," *Physics of Fluids A: Fluid Dynamics*, vol. 4, pp. 1510-1520, 7 1992.
- [22] Z. Yang and T. H. Shih, "New time scale based k-epsilon model for near-wall turbulence," *AIAA Journal*, vol. 31, pp. 1191-1198, 7 1993.
- [23] D. C. Wilcox, Turbulence modelling for CFD, 2nd ed. ed., La C nada, Calif: DCW Industries, 1998.
- [24] F. R. Menter, "Two-equation eddy-viscosity turbulence models for engineering applications," *AIAA Journal*, vol. 32, pp. 1598-1605, 8 1994.
- [25] B. P. Leonard, "A stable and accurate convective modelling procedure based on quadratic upstream interpolation," *Computer Methods in Applied Mechanics and Engineering*, vol. 19, pp. 59-98, 6 1979.
- [26] Ansys-Fluent, "ANSYS Fluent Theory Guide," 2015.
- [27] F. Ries, J. Janicka and A. Sadiki, "Thermal Transport and Entropy Production Mechanisms in a Turbulent Round Jet at Supercritical Thermodynamic Conditions," *Entropy*, vol. 19, p. 404, 8 2017.
- [28] D. C. Wilcox, Turbulence modeling for CFD, 3rd ed. ed., La C nada, Calif: DCW Industries, 2006.